Stabilization mechanism for the polar ZnO(000$\bar{1}$)-O surface

Roman Wahl,[1] Jeppe V. Lauritsen,[2] Flemming Besenbacher,[2] and Georg Kresse[1]

[1]*Faculty of Physics, Universität Wien and Center for Computational Materials Science, Sensengasse 8/12, A-1090 Wien, Austria*

[2]*Interdisciplinary Nanoscience Center (iNANO) and Department of Physics and Astronomy, Aarhus University, Denmark*

When wurtzite ZnO is sliced perpendicular to the (0001) axis, two different polar surfaces, the (0001)-Zn and (000$\bar{1}$)-O terminated surfaces, are formed. In a simple ionic picture, both surfaces are electrostatically unstable due to a diverging electrostatic energy. Although the ionic picture is an oversimplification, the surfaces adopt a modified surface structure to compensate for the polarity. In close collaboration with experiment, a hexagonal honeycomblike reconstruction has been suggested [J. V. Lauritsen *et al.*, ACS Nano **5**, 5987 (2011)]. The remarkable observation is that the (000$\bar{1}$)-O surface behaves very differently than the (0001)-Zn surface. Here, we present a detailed density functional theory investigation of the (000$\bar{1}$)-O surface, including a systematic investigation of H and Zn coverage as well as an investigation of various surface reconstructions. The difference between the two polar surfaces is explained by the different bonding preferences of Zn and O atoms: as a *d* element, Zn atoms are more flexible in their bond formation than O atoms.

I. INTRODUCTION

It is impossible to trace back the first use of zinc oxide (ZnO) since zinc oxide has already been utilized by early humans. Until the 20th century, the main application of ZnO was as an ingredient in medical ointments and as pigments in paints, especially in zinc white. Today, ZnO is usually processed in its white powder form, and it is used as additive in many materials, such as plastic, glass, and rubber.

The crystal form of ZnO (zincite) is very rare on Earth and almost all commercially and scientifically utilized crystals are produced synthetically. It is a semiconducting transparent metal oxide crystal with a direct band gap of $\approx$3.3 eV (Ref. 1) and an interesting combination of semiconducting and optical properties. Although it is used in a wide range of applications such as optoelectronics, light-emitting devices, and catalysis,[2] the fundamental principles concerning the structure and reconstruction mechanisms of plain ZnO surfaces are still not explained adequately.

Bulk ZnO is built by stacking consecutively hexagonal layers of oxygen and zinc along the crystallographic *c* or (0001) axis with alternating distances of $R_1 = 0.61$ Å and $R_2 = 1.99$ Å (see Fig. 1). When cleaving the ZnO crystal perpendicular to this axis, two principally different surfaces are created. The oxygen terminated (000$\bar{1}$) surface, on which we will focus our investigations, and the zinc terminated (0001) surface, which was already investigated recently.[3–5] Both of them are polar, belong to the so-called "Tasker-type(3)" surfaces,[6] and are attributed to be unstable in their bulk-terminated ideal form due to a diverging electrostatic surface energy. Polar surfaces can be stabilized by modifying either the charge or the stoichiometry in the surface layers with respect to the bulk. Different mechanisms are conceivable to compensate for the instability of the bulk-terminated surface. Surface atoms can desorb, leading to reconstructions of the surface. Atoms from the residual atmosphere in the experimental setup can adsorb on the surface, providing the necessary charge compensation. Finally, charge transfer within the material under consideration may happen as response to the polar electrostatic field, yielding partially ionic surface species and metallic surface states.[7] The latter mechanism, also referred to as "metallization of the polar surfaces," was not observed in a recent scanning tunneling spectroscopy (STS) experiment on ZnO.[8]

Here, we investigate in detail possible reconstructions on the (000$\bar{1}$)-O terminated surface within the density functional theory (DFT) framework as implemented in the VASP program.[9,10] The results of these calculations on the different surface terminations are then used for the construction of a comprehensive phase diagram. We note that we have not included vibrational entropy in this study, although it is expected to modify the surface phase diagram to some extent.[4] The corresponding calculations would be fairly involved and are left for future studies.

In Sec. II, we will briefly explain our computational setup and we will introduce the formalism used in the thermodynamics and the calculation of the phase diagram. The results of all considered stabilization mechanisms are presented in Sec. III, and final remarks and the conclusions are given in Sec. IV.

II. COMPUTATIONAL DETAILS

The first step towards an accurate simulation of surfaces is the calculation of the theoretical lattice parameters of bulk ZnO. We used the PW91,[11,12] the PBE,[13] PBEsol,[14] and HSE06 (Ref. 15) hybrid exchange-correlation (xc) functionals for these calculations. The cutoff energy for the plane-wave basis set was chosen to be 600 eV, and the internal parameters as well as the lattice constants were carefully relaxed. To obtain converged parameters, in particular an accurate c/a ratio, a dense $16 \times 16 \times 16$ Γ-centered *k*-point mesh was used.

When the calculated equilibrium lattice parameters are compared to experiment (see Table I), similar trends as in Ref. 17 for SrTiO$_3$ and BaTiO$_3$ can be observed: PBEsol improves the lattice parameter *a* compared to the standard PW91 and PBE functionals, but it has no effect on the c/a ratio and the internal lattice parameter *u*. Only the HSE06 functional improves all important structural parameters
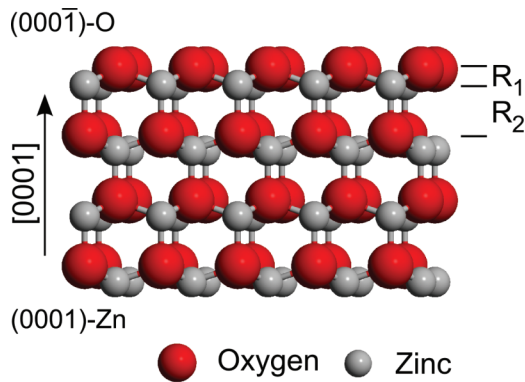
FIG. 1. (Color online) Ball and stick model of the ZnO structure (side view). ZnO adopts alternating hexagonal layers of fourfold-coordinated Zn and O atoms with alternating distances of $R_1 = 0.61$ Å and $R_2 = 1.99$ Å.

simultaneously, however, it is very expensive for large-scale surface calculations considered in this work.

Overall, it is clear that the second best choice, and the best choice among the pure density functionals, would be the PBEsol functional. This functional is designed to give an improved description of the lattice parameters of solids, but also yields accurate surface energies. However, we decided to use the PW91 xc functional throughout our calculations to maintain compatibility to the previous studies on the (0001)-Zn terminated surface side.[3,4] The applied projector augmented wave (PAW) potentials are also identical to the previous work.[3]

A. Setup of surface calculations

Since large supercells are needed to model different surface reconstructions, a compromise between calculational accuracy and computational parameters such as slab size or vacuum width has to be made.

For the construction of the phase diagram, the quantity of interest is the change of the surface energy $\Delta\gamma$ [see Eq. (1)]. To judge the reliability of a chosen set of simulation parameters, we calculated the change of the surface energy for two different surface reconstructions versus the number of ZnO double layers: the vacuum width and the cutoff energy.

The chosen reference system is a (1×2) supercell with one (coverage $c_v = 0.5$) and two oxygen surface atoms ($c_v = 1.0$) removed from the topmost surface layer. For all considered

TABLE I. Lattice parameter a and the c/a ratio of bulk ZnO for different exchange-correlation functionals. Additionally, the parameter $u = R_2/c$ (see Fig. 1) is shown, determining the relative position of the oxygen and zinc sublattices along the (0001) axis. The numbers in parentheses are the deviations from the corresponding experimental values in percent.

	a		c/a		u	
PW91	3.283	(+1.0)	1.615	(+0.8)	0.3788	(−0.7)
PBE	3.287	(+1.2)	1.614	(+0.8)	0.3790	(−0.7)
PBEsol	3.237	(−0.4)	1.615	(+0.8)	0.3787	(−0.8)
HSE06	3.259	(+0.3)	1.607	(+0.3)	0.3803	(−0.3)
Expt. (Ref. 16)	3.249		1.602		0.3816	

slabs, we set out from a clean, bulk-terminated unreconstructed surface and allowed the three outermost double layers on both sides of the slab to relax.[3,5] Only for the slabs with six double layers thickness, two double layers on each side were relaxed. For the calculations where one or two oxygen surface atoms were removed, we used the clean relaxed slabs as a starting point, removed the corresponding number of oxygen atoms from the surface layer, and held the Zn terminated (0001) surface layer fixed during the structural optimization.

Additionally, we introduced the two following modifications to the Zn atoms on the Zn terminated side to accelerate the layer convergence and reduce the compute time:

(i) The Zn surface atoms were replaced by artificial atoms[3,5] with the valency set to 1.5. This makes the surface essentially stoichiometric and autocompensated, i.e., the surface is semiconducting and possesses no holes in the valence band or electrons in the conduction band. Similar procedures are often adopted to passivate dangling bonds on semiconductor surface, although it is more common to adsorb pseudo-hydrogen atoms with a proper valence at the side that requires termination and passivation.[18]

(ii) In the topmost four Zn layers, the Zn s and the semicore Zn d electrons were treated as valence electrons, resulting in 12 valence electrons per Zn atom. In the deeper layers, the Zn d electrons were placed in the core, and only the two Zn s electrons were treated as valence orbitals. The positions of these ions were kept fixed to the positions determined using the conventional potentials. This approach is justified because the Zn semicore d electrons are well localized and hybridize only fairly little with the Zn s and oxygen p electrons. Similar approaches are commonly used in quantum chemistry calculations to reduce the number of electrons. In our case, this approximation allows us to reduce the number of valence electrons by a factor 1.5 to 2, drastically reducing the computational requirements without a notable impact on the final results.

We calculated the change of the surface energy for the two structures mentioned above in dependence on the number of double layers of zinc and oxygen, at two different cutoff energies, 280 and 400 eV, and with different vacuum widths (8, 10, and 14 Å). For all calculations, a $(12 \times 6 \times 1)$ Γ-centered k-point mesh was used.

As shown in Fig. 2, the change of the surface energy shows almost identical convergence with respect to the slab thickness and cutoff energy for both surface terminations ($c_v = 0.5$ and 1.0), and the cutoff energy has only a tiny influence on the energy (we note that the broken curves for $c_v = 1.0$ are shifted by 2.59 J/m²). Similar to the observation in Ref. 3, a significantly faster convergence with respect to the slab thickness is achieved by reducing the valence of the outermost "Zn" atoms on the (0001)-Zn side to 1.5 using the artificial Zn pseudoatom. As already mentioned, this makes the (0001)-Zn surface side semiconducting, avoiding charge transfer from this surface to the investigated (000$\bar{1}$)-O side. Using this compensated slab, 8 double layers of ZnO yield almost the same change in the surface energy as 18 double layers for the uncompensated slab.

For the final calculations, the thickness of the slab was fixed to eight double layers of ZnO with the outermost
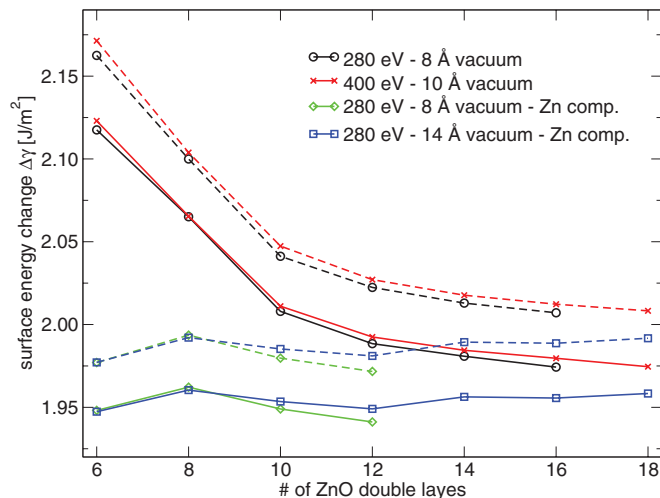
FIG. 2. (Color online) Change of the surface free energy compared to bulk-terminated surface for two (1×2) surface unit cells with an oxygen vacancy concentration of $c_v = 0.5$ (solid line) and $c_v = 1.0$ (broken line) for different vacuum widths and cutoff energies. The broken lines ($c_v = 1.0$) were shifted downwards by 2.59 J/m^2 to allow for presentation on a single plot. The calculations marked as "Zn comp" use a Zn atom with a valence of 1.5 on the (0001) surface side to autocompensate that surface.

"Zn" atoms on the (0001) side possessing a partial valency of 1.5. A vacuum width of 8 Å was adopted since the difference to 14 Å was only of the order of 0.02 J/m^2, and the cutoff energy was set to 280 eV. This choice represents a well-balanced compromise between calculational accuracy and computational efficiency, and we expect our results to be converged within 0.02 J/m^2. Relative differences in the surface energies at similar stoichiometries are most likely even more accurate. In addition, we performed for the two most stable structures [(2×2) and (5×5)] test calculations using a harder O potential and a cutoff energy of 400 eV and found that the total energy changes by less than 1 meV per unit cell upon further relaxation, corroborating the accuracy of the present computational setup.

B. Thermodynamics of the (000$\bar{1}$)-O surface

If we are interested in equilibrium properties and consider the kinetics to be sufficiently fast, we can use standard equilibrium thermodynamics. The formalism we use here is already well established in the surface science community ("*ab initio* thermodynamics"), and a very detailed discussion can be found in previous work.[3,19,20] In the following, we will briefly introduce the main equations (for further reading, we refer to Refs. [3], [20], and [21]).

The thermodynamic quantity of interest to determine the stability is the change in the surface free energy per surface area. Using standard thermodynamics, it can be shown that the change in the surface free energy can be approximated as

$$\Delta\gamma(\mu_O, \mu_H) = \frac{1}{A}\Big[E_{slab} - E_{slab\text{-}reference} - n_H^{add}\mu_H$$
$$+ n_{Zn}^{vac}E(ZnO) + (n_O^{vac} - n_{Zn}^{vac})\mu_O\Big], \quad (1)$$

if zero-point vibrations, vibrational entropy contributions, and enthalpy changes are neglected and assuming that bulk ZnO is in thermal equilibrium with the surface. Here, A is the surface area per supercell, E_{slab} is the energy of the considered slab, $E_{slab\text{-}reference}$ is the energy of the reference bulk-terminated slab, $E(ZnO)$ is the energy of bulk ZnO (per formula unit), n_{Zn}^{vac} and n_O^{vac} are the number of removed zinc and oxygen atoms compared to the reference slab, and n_H^{add} is the number of adsorbed hydrogen atoms. The only unknowns are then the chemical potentials of oxygen μ_O and zinc μ_{Zn}. Nevertheless, care has to be taken since in a recent work[4] it has been shown that the vibrational entropy of the (0001)-Zn surface can play a decisive role at elevated temperatures, when different surface terminations with similar slope in the phase diagram are close to each other within a narrow energy range. As already mentioned, we have not considered this in this work, which implies that the present phase diagrams are only valid at low temperatures where vibrational contributions are small. Furthermore, we have also neglected zero-point vibrations.

C. Reference energies

As we will see in the next section, binding and total energies of the hydrogen and oxygen dimers, as well as of bulk ZnO and hexagonal Zn, are needed for the determination of the change in the surface free energy and boundaries of the phase diagrams in dependence on the oxygen and hydrogen partial pressures. Here, we briefly summarize the required reference energies.

All structures under consideration were initially fully optimized using a cutoff energy of 600 eV. For the molecules, a large unit cell was chosen to reduce the effect of the periodic boundary conditions. For the bulk systems, a $16 \times 16 \times 16$ Γ-centered k-point mesh was used, and for the free atoms and molecules, the Γ point only was used. After the geometry optimization, the cutoff for bulk ZnO and Zn was reduced to 280 eV to match the cutoff used throughout the slab calculations and the total energies E were recalculated without further geometry optimization.

For the calculation of the atomization energies D, the energies of symmetry-broken atoms $E(X)$ are needed (Table II):

$$D = -E + \sum_X E(X). \quad (2)$$

For the hydrogen, the oxygen atom, and the oxygen dimer, a spin-polarized symmetry-broken calculation was used to properly account for their ground states, Hund's rule, and the paramagnetic state of O$_2$. The oxygen PAW potential used in this work is well suited for slab calculations. However, when used for the oxygen dimer, the bond length is too large by 8.5%

TABLE II. Energies for single symmetry-broken spin-polarized atoms H, O, and Zn, calculated with respect to the VASP energy reference (symmetric spherical atom). All calculations performed at 280 eV, except for O^{hard}, where 800 eV were used.

(eV)	H	O	O^{hard}	Zn
E	-1.11	-1.787	-1.846	0.00

TABLE III. Calculated energies E (as determined by VASP) and atomization energy D for the H$_2$ and O$_2$ molecules and for bulk hexagonal Zn and ZnO (all determined at 280 eV, except for the column O$_2^{\text{hard}}$, where the hard PAW potential was used at 800 eV). In addition, theoretical values and experimental heats of formation (D_{expt}) are reproduced from Ref. 22 for comparison. Energies are specified per formula unit.

(eV)	H$_2$	O$_2^{\text{hard}}$	Bulk Zn	Bulk ZnO
E	-6.74	-10.00	-1.11	-9.02
D	4.52	6.31	1.11	2.97
Ref. 22	4.50	6.61	1.12	2.84
D_{expt}	4.52	5.17	1.35	3.50

in comparison to the experimental value of 1.21 Å. Therefore, a much "harder" PAW potential with a core radius of 0.582 Å for the s and p orbitals and a cutoff of 800 eV is used for the reference calculations on the oxygen atom and dimer. With this "hard" potential, the deviation from the experimental bond length can be reduced to 0.8%.

Table III shows the data obtained within this study and the theoretical values and experimental heats of formations from Ref. 22 for comparison. As described above, a different potential and cutoff were applied for the oxygen dimer, and this requires some further considerations for relative energies. Whenever we require a reference energy for the oxygen dimer, we replace the value give in Table III by

$$E\left(O_2^{\text{hard}}\right) - 2E(O^{\text{hard}}) + 2E(O) = -9.879 \text{ eV}. \quad (3)$$

This minimizes errors introduced by different cutoffs and potentials used for the oxygen dimer. All calculations for the hard potential were performed at 800 eV, whereas all calculations involving the standard soft oxygen potential are performed at 280 eV.

As one can see, our results are in overall good agreement with the former calculations of Meyer,[22] but we find stronger binding for bulk ZnO and weaker binding for O$_2$, which we attribute to more accurate potentials. Furthermore, the present calculations agree well with previous calculations by Paier *et al.*[23] using the VASP and the Gaussian codes.

D. Phase diagram

In principle, the most stable surface reconstruction at a given temperature and partial pressure of components x in the gas phase can be found by performing an unconstrained minimization of Eq. (1). Due to the lack of suitable global search algorithms for large-scale reconstructions, it is common practice to investigate a number of suitable reconstructions based on chemical intuition and to determine the one with the lowest surface energy.

For each type of surface reconstruction, we calculated the change in the surface free energy $\Delta\gamma$ at the conditions imposed by the chemical potentials μ_O and μ_H. Using these values, we can build a two-dimensional surface phase diagram, where the two axes correspond to the chemical potential of oxygen and hydrogen, respectively. Each reconstruction is assigned a unique color in the phase diagram to visualize the phase

with the lowest surface free energy at a given set of chemical potentials.

It is important to keep in mind that we might have overlooked possible reconstructions. To reduce this risk, we considered a fairly large number of different surface terminations and reconstructions and, furthermore, we used the available experimental input to guide our search for low-energy structures.

It is common practice to reference all energies and chemical potentials to half the binding energy of the molecules under consideration, i.e.,

$$\Delta\mu_O = \mu_O - 1/2E(O_2), \quad \Delta\mu_H = \mu_H - 1/2E(H_2). \quad (4)$$

This implies that the hydrogen and oxygen molecules have zero chemical potential $\Delta\mu_O$, $\Delta\mu_H$ at $T = 0$ K. Using Eq. (4), we can rewrite Eq. (1) to

$$\Delta\gamma(\Delta\mu_O, \Delta\mu_H)$$
$$= \frac{1}{A}\Big[E_{\text{slab}} - E_{\text{slab-reference}} - n_H^{\text{add}}[\Delta\mu_H + 1/2E(H_2)]$$
$$+ \left(n_O^{\text{vac}} - n_{Zn}^{\text{vac}}\right)[\Delta\mu_O + 1/2E(O_2)] + n_{Zn}^{\text{vac}}E(ZnO)\Big]. \quad (5)$$

For the oxygen dimer energy, we use the redefined value given in Eq. (3); a change of the oxygen reference energy will, however, only cause a constant shift of all phase boundaries by half the change of the oxygen dimer energy, leaving the constructed phase diagram otherwise unmodified. The bounds of the chemical potentials for Zn, O, and H are chosen along the lines discussed in Ref 3:

$$-3.0 \text{ eV} < \Delta\mu_O < 0.0 \text{ eV},$$
$$-3.0 \text{ eV} < \Delta\mu_H < 0.0 \text{ eV}, \quad (6)$$
$$\Delta\mu_O + 2\Delta\mu_H < -2.61 \text{ eV}.$$

The last equation determines the phase boundary for the formation of water.

E. Pressure and temperature dependence of the chemical potentials

For comparison of the phase diagram calculated from *ab initio* with the experimental findings, it is helpful to know the temperature and pressure dependence of the chemical potentials used in the phase diagram

$$\mu_x(T, p_x) = \mu_x^0(T, p_0) + \frac{1}{2}k_BT\ln\left(\frac{p_x}{p_0}\right), \quad (7)$$

essentially the ideal gas equation. We refer to Ref. 20 (Sec. II E) for further details.

III. RESULTS

A. Compensation mechanisms

Since oxygen has a significantly larger electron affinity than zinc, it is expected that in bulk ZnO the two 4s valence electrons of zinc are transferred to the oxygen atoms, creating a closed oxygen 2p shell. In the bulk material, each Zn ion is surrounded by four oxygen atoms, hence, in average, half an electron is transferred along each bond to a neighboring oxygen ion, and no long-range charge transfer is required to reach a fully ionic state.

The situation changes at the bulk-terminated clean (0001) and (000$\bar{1}$) surfaces. Regardless of the surface side, each topmost ion in the surface layer has only three next-nearest neighbors. Therefore, at the (0001) terminated surface, the ionicity of the zinc surface ions is reduced to $Zn^{+3/2}$, whereas at the (000$\bar{1}$) terminated side, oxygen has an ionicity of $O^{-3/2}$ and a closed $2p$ shell can not be reached. This partial ionicity of $\pm 3/2$ forces electrons at the (0001)-zinc terminated side into the conduction band, whereas the valence band is not entirely filled at the ideal (000$\bar{1}$)-oxygen terminated side. Although these conclusions are drawn from an oversimplified atomistic picture, this model was confirmed to be applicable to ZnO (see Ref. 3) and also to be the main reason for the lower stability of polar surfaces in comparison to their nonpolar counterpart. Lowering of the surface energy can be achieved preferably by changing the surface stoichiometry by removing a certain amount of oxygen and zinc atoms from the surface layer or by adsorbing hydrogen at the oxygen surface atoms.

In the following, we will investigate the stability of the (000$\bar{1}$)-O terminated surface with respect to "randomly" distributed oxygen vacancies. In a second step, we introduce hydrogen on the clean unreconstructed surface. Then, we will focus on the simultaneous creation of oxygen and zinc vacancies, which is essential in order to realize more complex surface reconstructions such as triangles and hexagonal holes.

B. Oxygen vacancies

As mentioned in the preceding Introduction, the polar (000$\bar{1}$)-O terminated ZnO surface is supposed to be stabilized by depleting oxygen from the surface. The quantity of interest is the change of the surface free energy with respect to the surface energy of the bulk-terminated slab. Using Eq. (5), we obtain

$$\Delta\gamma(\Delta\mu_O)$$
$$= \frac{1}{A}\left[E_{slab}^{O\text{-}vac} - E_{slab\text{-}reference} + n_O^{vac}[\Delta\mu_O + 1/2E(O_2)]\right].$$
$$(8)$$

In a recent study, Meyer[22] investigated the behavior of the surface free energy in dependence of the oxygen chemical potential and the concentration of oxygen vacancies in the surface layer within a (2×2) supercell. It is evident that a restriction to a (2×2) supercell leads to a very limited number of surface structures, which are, in addition, highly periodic and perfectly ordered. It is likely that surface reconstructions exist that are lower in energy since pits and islands are found to be stable on the Zn terminated (0001) surface.[3]

To extend the set of possible surface vacancy structures, we expanded our calculations to a (4×4) supercell, which is four times larger than the previously used supercell. This approach has two major benefits: first, we are able to investigate the gradual increase of the vacancy concentration in dependence on the oxygen partial pressure in greater detail. Second, for a given oxygen vacancy concentration, the number of possible vacancy arrangements increases drastically. For example, at a vacancy concentration of $c_v = \frac{1}{4}$, only one possible vacancy structure can be realized for the (2×2) supercell, whereas seven symmetry inequivalent structures exist in the (4×4) supercell.
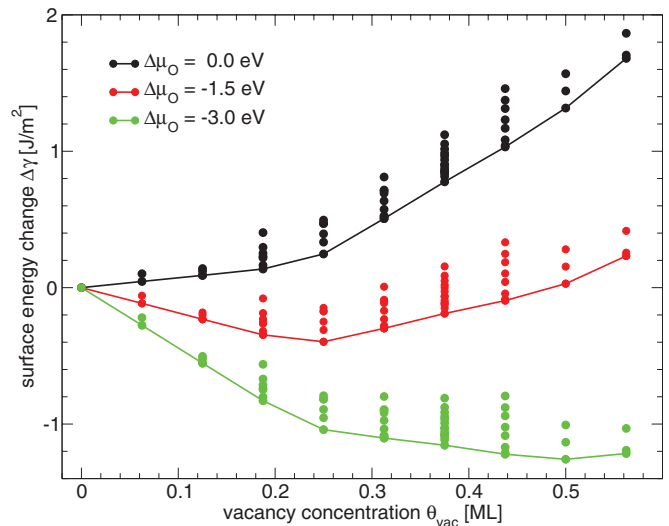

FIG. 3. (Color online) Change in the surface energy $\Delta\gamma$ in dependence of the oxygen vacancy concentration θ_{vac} for three different oxygen chemical potentials. Each of the 73 considered surface terminations is denoted by a filled circle and the lowest ones are interlinked by solid lines. Only points lying on a convex hull are stable. The chemical potential at which a certain phase is stable can be determined by drawing a tangent to the convex hull and calculating the intersections with the y axis (Legendre transformation).

In total, we investigated 73 different configurations of oxygen vacancies for different concentrations. To determine the most stable structures, we plot the change in the surface free energy with respect to the oxygen vacancy concentration, as given in Fig. 3, for three different oxygen chemical potentials. The variable transformation from the oxygen chemical potential $\Delta\gamma(\Delta\mu_O)$ as given in Eq. (8) to the oxygen vacancy concentration $\Delta\gamma(\theta_{vac})$ can be performed via a Legendre transformation:

$$\frac{d\Delta\gamma(\Delta\mu_O)}{d\Delta\mu_O} = \frac{n_O^{vac}}{A} = \theta_{vac},$$

$$\Delta\gamma^*(\theta_{vac}) = \Delta\gamma(\Delta\mu_O) - \Delta\mu_O\theta_{vac}$$
$$= \frac{1}{A}\left(E_{slab}^{O-vac} - E_{slab\text{-}reference}\right) + \frac{1}{2}\theta_{vac}\,\overline{E}(O_2).$$
$$(9)$$

The chemical potential is absent from this equation and has been accommodated in the oxygen reference energy $\overline{E}(O_2)$. For oxygen-rich conditions ($\overline{E}_{O_2} = E_{O_2}$), no energy is gained by removing oxygen from the surface since oxygen is abundantly available in the gaseous environment. When lowering the reference energy corresponding to a reduction of the oxygen partial pressure, the formation of oxygen vacancies becomes energetically favorable. For $\overline{E}_{O_2} = E_{O_2} - 1.5$ eV, the change in the surface energy drops until a vacancy concentration of 0.25 monolayers (ML) is reached. When depleting the surface layer further, the surface energy increases again. In the Zn-rich regime ($\overline{E}_{O_2} = E_{O_2} - 3.0$ eV, corresponding to the onset of ZnO decomposition into metallic Zn), the energy change drops until half of the surface layer is depleted.

Additionally, we see that the change of the slope of the convex hull is largest at a quarter vacancy concentration.
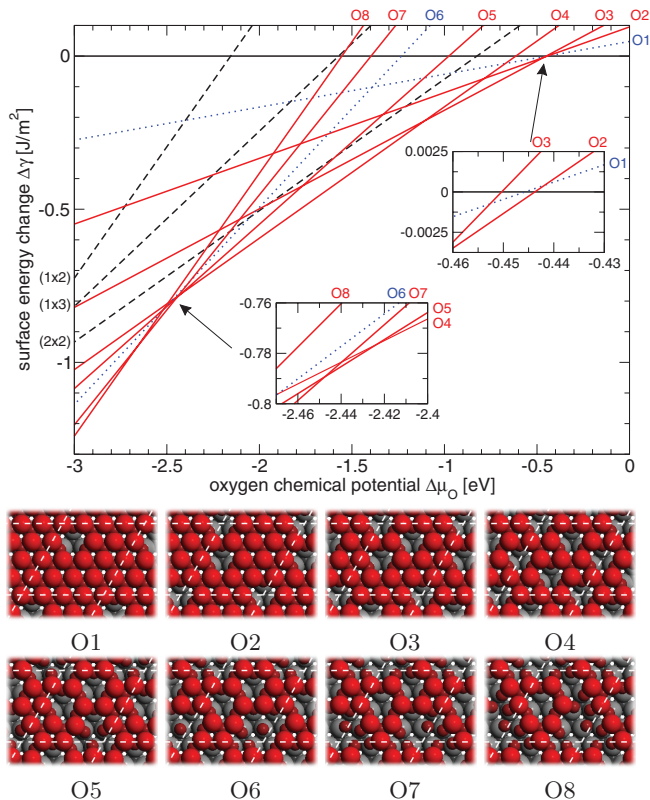
FIG. 4. (Color online) Surface free energies as a function of the chemical oxygen potential for the most stable vacancy configurations. The black broken lines show our data using the configurations of Ref. 22 including the (1×3) missing oxygen row structure (see labels on the left). In the insets, crucial areas are magnified, where the blue dotted lines mark the phases with concentrations of $\frac{1}{16}$ and $\frac{6}{16}$ which do not show up in the phase diagram. Below the diagram, we present the corresponding ball models of the vacancy configurations for concentrations of $c_v = \mathrm{O}n/16$.

Therefore, this surface reconstruction is particularly stable in a wide range of the chemical potentials $\Delta\mu_{\mathrm{O}}$. Another feature we can extract from Fig. 3 is whether a reconstruction will appear in the phase diagram: if a phase lies above the convex hull, the reconstruction will not be present in the phase diagram.

In Fig. 4, we present the energy of the most stable configurations versus the chemical potential, together with the free-energy curves of the structures reported in Ref. 22 (black broken lines). In comparison to Meyer,[22] we find significantly more favorable vacancy configurations by lifting the constraint to (2×2) surface unit cells. In the case of a vacancy concentration of $\frac{1}{4}$, the present structure shown in the lower panel (O4) in Fig. 4 is 0.091 J/m² lower in energy than the previously considered structure, and for the vacancy concentration of $\frac{1}{2}$ the energy difference in favor to the present structure (O8) is 0.516 J/m².

In addition, we find a fairly smooth increase of the oxygen vacancy concentration with decreasing oxygen chemical potential, although the structure at $c_v = \frac{1}{4}$ is stable over a wide range of 1.32 eV. Note again that some vacancy concentrations ($\frac{1}{16}$ and $\frac{6}{16}$) are unstable, but given the error bars of the present calculations, we do not put a too strong emphasis on this result.

The phases that show up in the phase diagram are shown schematically as ball models in Fig. 4. The images suggest that hexagonal ring structures for the remaining oxygen atoms are preferred. When the vacancy coverage increases beyond $\frac{4}{16}$, these rings start to break up, but some rings prevail until the maximum vacancy concentration of $\frac{8}{16}$ is reached.

Low-energy electron diffraction (LEED) and helium atom scattering (HAS) experiments performed by Kunat *et al.*[24] indicate the presence of a (1×3) structure for the O terminated surface in an almost hydrogen-free environment (see Ref. 25 for a recent review). The proposed structure was investigated by Meyer[22] and was re-considered in this work. However, as already observed by Meyer, our calculations do not corroborate the stability of the missing row (1×3) structure. In fact, this structure is higher in energy by about 0.25 J/m² than comparable structures (O5 and O6) at similar stoichiometries (see broken line in Fig. 4). Moreover, a recent LEED experiment relates the (1×3) surface termination possibly to the presence of impurities in the surface,[8] although we note that Wöll carefully checked for the existence of contaminating impurities.[25]

C. Hydrogen adsorption

The adsorption of hydrogen on the $(000\bar{1})$-O surface is an alternative compensation mechanism, and since residual hydrogen is usually present in the UHV chamber and under all practical conditions where ZnO is processed, or via diffusion from bulk interstitial sites, it is worthwhile to investigate the influence of hydrogen on the phase diagram.

Hydrogen molecules H_2 can adsorb or dissociate from the surrounding atmosphere or become available from the bulk, forming OH^- groups. In principle, there are three different possible sites for the formed OH^- groups. The conventional bulk continuation of ZnO (hcp hollow), the fcc continuation with no Zn underneath, and an on-top position atop a Zn atom in the layer underneath. We calculated the total energy of all surface models at zero, half, and full hydrogen coverage, and the corresponding energies for the fcc hollow and on-top structure compared to the energy of the bulk continuation (hcp hollow) are presented in Table IV.

For zero hydrogen concentration c_H, the conventional hcp hollow positions are the most stable site for the oxygen surface atoms (bulklike continuation). Covering the surface with a (2×1) overlay of hydrogen (Fig. 6, H8), the hcp hollow

TABLE IV. Total energy in eV for hydroxyl groups OH^- on the $(000\bar{1})$ surface. Energies are specified with respect to normal bulk continuation (hcp). As alternative OH adsorption sites, we considered the position on top of the underlying Zn atoms and in the Zn fcc hollow position. The clean oxygen surface layer ($c_H = 0.0$), as well as half coverage ($c_H = 0.5$), and a full monolayer coverage of hydrogen ($c_H = 1.0$) were considered. The numbers in parentheses are theoretical values from Ref. 22 for comparison.

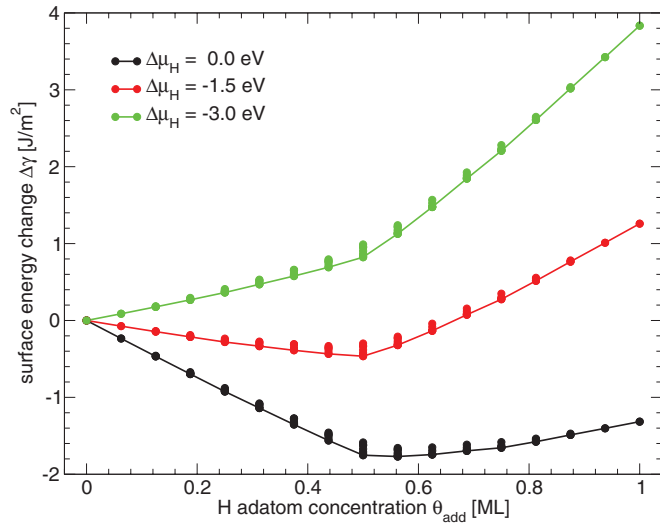| c_H	On top		hcp hollow	fcc hollow	
0.0	+3.009	(+3.16)	0.00	+0.044	(+0.05)
0.5	+2.826		0.00	+0.008	
1.0	+1.784	(+1.78)	0.00	−0.006	(−0.02)

FIG. 5. (Color online) Change of the surface energy $\Delta\gamma$ in dependence on the hydrogen concentration θ_{add} for three different hydrogen chemical potentials. Each of the 76 considered surface terminations is denoted by a filled circle and the lowest ones are interlinked by solid lines.

site is still the preferred position, however, the difference between the hcp and fcc hollow sites is now almost zero. When entirely covering the surface with hydrogen atoms, the preferred oxygen surface site changes from Zn-hcp to the Zn-fcc hollow site. Again, the energy difference is almost zero and not relevant on the scale we are considering in Fig. 6. Hence, we performed the majority of the calculations with oxygen at the hcp site in a (4 × 4) supercell. The change of the surface free energy with respect to the bulk-terminated slab can be deduced from Eq. (5):

$$\Delta\gamma(\Delta\mu_H)$$
$$= \frac{1}{A}\big[E_{slab}^{\text{H-add}} - E_{\text{slab-reference}} - n_H^{\text{add}}[\Delta\mu_H + 1/2E(H_2)]\big].$$
(10)

In total, we investigated 76 surface configurations (see Fig. 5) and similarly to Sec. III B, we first present the surface energy change versus the hydrogen concentration:

$$\frac{d\Delta\gamma(\Delta\mu_H)}{d\Delta\mu_H} = -\frac{n_H^{\text{add}}}{A} = -\theta_{add},$$
$$\Delta\gamma^*(\theta_{add}) = \Delta\gamma(\Delta\mu_H) + \Delta\mu_H\theta_{add}$$
$$= \frac{1}{A}\big(E_{slab}^{\text{H-add}} - E_{\text{slab-reference}}\big) - \frac{1}{2}\theta_{add}\,\overline{E}(H_2).$$
(11)

In a hydrogen-rich gaseous environment ($\overline{E}_{H_2} = E_{H_2}$), hydrogen will adsorb on the surface. The maximum in the change of the surface energy is reached at an adatom concentration of $\frac{9}{16}$. When the hydrogen chemical potential is reduced ($\overline{E}_{H_2} = E_{H_2} - 1.5$ eV), which is equivalent to a reduction of the amount of hydrogen in the gas phase, an adatom concentration of $\frac{1}{2}$ yields the largest change in the surface energy. Reducing the chemical potential of hydrogen even further ($\overline{E}_{H_2} = E_{H_2} - 3.0$ eV), adsorption of hydrogen becomes energetically unfavorable. From the convex hull, we

can deduce that the surface covered by half a monolayer of hydrogen is a particularly stable surface termination in a fairly large range of hydrogen chemical potentials $\Delta\mu_H$.

Arranging the hydrogen atoms on the surface of a (4 × 4) supercell is more straightforward than arranging the oxygen vacancies in Sec. III B. Also, energy differences between different configurations at one specific coverage are much smaller than for oxygen. As intuitively expected, maximizing the distance between the individual hydrogen adatoms is the key factor to minimize the surface energy. Reconstructions with closely packed hydrogen clusters are always higher in energy than configurations that maximize the distance between the OH⁻ complexes. Patterns with intermediate, H-uncovered oxygen atoms can only be constructed until a hydrogen concentration of $c_H = \frac{1}{4}$ is reached. At $c_H = \frac{1}{4}$, the most stable configuration possesses a (2 × 2) periodicity (see Fig. 6, H4). When further increasing the concentration of hydrogen, H has to adsorb on "interstitial" oxygen surface atoms, where a tendency to form parallel linear chains on the surface is observed. In fact, at half coverage, the most stable configuration is formed by placing hydrogen atoms in a "linear" (1 × 2) periodicity.

Figure 6 shows the change of the surface free energy in dependence on the hydrogen chemical potential relative to the clean (0001̄)-O surface. The respective hydrogen concentrations are shown above the corresponding red full lines. The black broken lines correspond to the data extracted from Fig. 3 of Ref. 22 for $c_H = \frac{1}{4}$ and $\frac{1}{2}$, which agree reasonably well with our results. In the inset, we zoomed in the area where most of the transitions between phases occur. At low hydrogen pressure (-3.0 eV $< \Delta\mu_H < -2.181$ eV), the clean surface (without hydrogen adsorbates) is the most

H2   H4   H6   H8
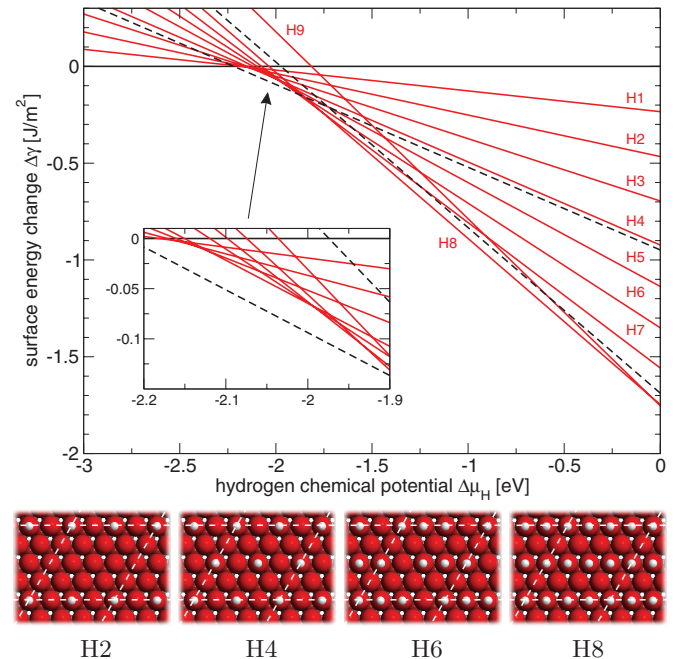
FIG. 6. (Color online) Change in the surface energy versus the chemical potential $\Delta\mu_H$ for different hydrogen concentrations on the (0001̄)-O terminated ZnO surface. The black broken lines correspond to the data extracted from Fig. 3 of Ref. 22 for $c_H = \frac{1}{4}$ and $\frac{1}{2}$.
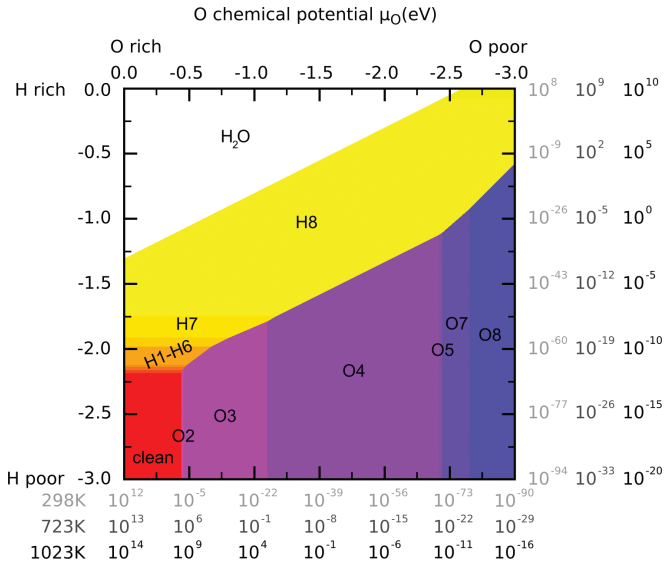
FIG. 7. (Color) Color-coded two-dimensional phase diagram of the O terminated ZnO-(000$\bar{1}$) surface as a function of O and H chemical potentials. Oxygen vacancies and hydrogen adatoms, as described in the text, were taken into account.

stable structure. By increasing the hydrogen partial pressure (-2.181 eV $< \Delta\mu_H < -1.766$ eV), a continuous increase of the adsorbed hydrogen coverage on the surface can be observed from $c_H = \frac{1}{16}$ to $\frac{7}{16}$. The most "stable" hydroxylated surface found in the phase diagram is the configuration that is half covered with hydrogen, which is expected since this configuration will yield a completely compensated surface. In the phase diagram, this structure is the favored termination over a range of 1.716 eV. Only at very high hydrogen partial pressures, the hydrogen coverage can be increased beyond half a monolayer ($c_H = \frac{1}{2}$). A hydrogen concentration beyond $c_H = \frac{9}{16}$ is not realized in our present calculations, which is in agreement with the maximum hydrogen coverage of 0.5 ± 0.05 found in Ref. 26.

In Fig. 7, we show the two-dimensional surface phase diagram as a function of both the oxygen and the hydrogen chemical potential. It is important to note that the oxygen chemical potential axis has been reversed in these plots (compared to Fig. 4). Additionally, we added at the bottom and to the right of the phase diagram for three temperatures the corresponding partial pressures to the oxygen and hydrogen chemical potential employing Eq. (7). The surface with zero vacancy concentration and no hydrogen adatoms adsorbed is depicted using the red color. When moving to higher oxygen vacancy concentrations, the color changes gradually from violet to blue, whereas it changes from orange to yellow when increasing the number of hydrogen adatoms. At hydrogen-rich conditions, half-hydrogen coverage is the most stable surface termination, independent of the oxygen partial pressure.

In general, our *ab initio* results, extrapolated to room temperatures and UHV pressures, coincide well with former theoretical findings[22] and with available experimental diffraction data, although we lack the (1×3) structure observed in HAS.[24,27] Experiments in the past were mostly carried out at room temperature and under UHV conditions. Under these conditions, both our present results and other previous studies

show that the O terminated ZnO surface quickly saturates with OH groups even in UHV. The surface then adopts a structure with half a monolayer OH [exemplified here by an ordered (1×2)H overlayer shown in Fig. 6, H8], which might well appear as a regular (1×1) structure in diffraction experiments due to the high mobility of the hydrogen atoms at the surface. This statement is, however, tentative, as we have not calculated entropic contributions or diffusion barriers for hydrogen mobility. As already explained, the previously observed (1×3) structure remains unaccounted.

D. Mixture of oxygen and zinc vacancies

In addition to the sole removal of surface oxygen atoms, as considered in Sec. III B, also a combination of oxygen and zinc removal can possibly lower the surface energy of the polar (000$\bar{1}$)-O surface. By removing the hydrogen dependence in Eq. (5), we obtain the change in the surface free energy as

$$\Delta\gamma(\Delta\mu_O) = \frac{1}{A}\left[E_{\text{slab}}^{\text{Zn,O-vac}} - E_{\text{slab-reference}} + n_{\text{Zn}}^{\text{vac}} E_{\text{ZnO}}^{\text{DFT}} \right.$$
$$\left. + \left(n_O^{\text{vac}} - n_{\text{Zn}}^{\text{vac}}\right)(\Delta\mu_O + 1/2 E_{O_2}) \right]. \quad (12)$$

To maintain a certain stoichiometry, the zinc and oxygen atoms must be removed in pairs. Vacancy clustering is then a consequence of minimizing the number of broken bonds. Initially, we adopted simple clustered vacancy structures as already discussed in Sec. III B, and removed as much zinc within the clustered vacancies as necessary to counterbalance the removal of up to four oxygen atoms. At the end, we investigated four different oxygen and zinc vacancy arrangements, including trapezoidal, rhomboidal, and hexagonal pits. All of them correspond to an effective oxygen vacancy concentration of $c_v = 0.25$. Ball and stick models and shorthands for these surface terminations are given in Fig. 8.

Energetically, all of the four structures are located close to each other in the phase diagram (Fig. 8). The structures O6Zn2 and O7Zn3 are energetically almost identical. The energy differences of the O5Zn1 and O6Zn2 structure to the O4 configuration are 0.147 and 0.103 J/m^2, respectively. Therefore, none of the investigated structures are energetically favorable and the simple oxygen vacancy O4 structure, already investigated in Sec. III B, remains the most stable surface termination for an oxygen vacancy concentration of $c_v = 0.25$.

However, none of the structures considered here follows the building rules for triangular reconstructions favored for the (0001)-Zn terminated side. Therefore, in the following section, we will focus our investigations on the triangular reconstructions adopted on the (000$\bar{1}$)-O surface side.

E. Triangular pits

Recent studies on the Zn terminated (0001) side of ZnO involving STM experiments and extensive large-scale DFT calculations[3,5] showed that the stabilization of the (0001)-Zn terminated surface is accomplished by removal of zinc and oxygen atoms of the first and second layers, resulting in the formation of triangular-shaped reconstructions. It is evident that this reconstruction mechanism can be adopted to the (000$\bar{1}$)-O surface by interchanging the Zn and O atoms. The
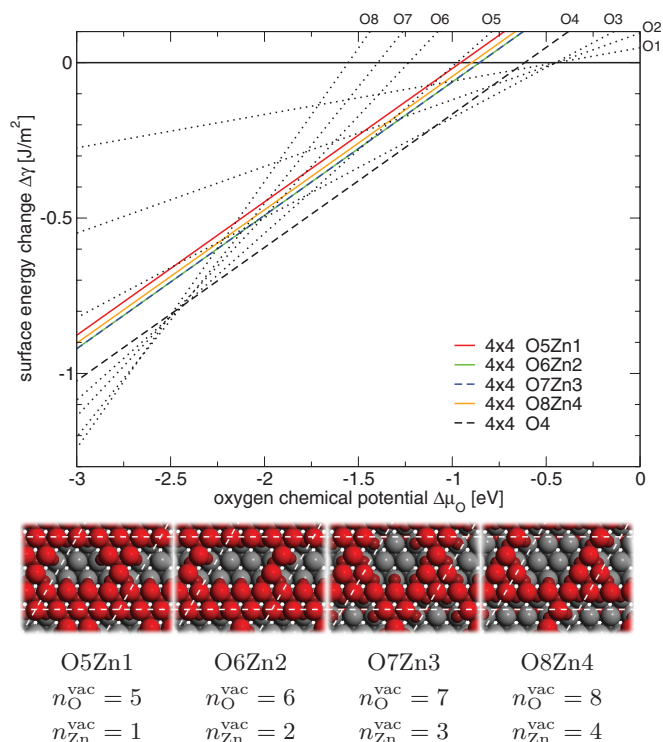
FIG. 8. (Color online) Surface energy as a function of the oxygen chemical potential for four surface terminations involving oxygen and zinc desorption from the first surface double layer with an effective oxygen vacancy concentration of $c_v = 0.25$. Underneath the phase diagram, ball and stick models and the corresponding abbreviations and the number of oxygen n_O^{vac} and zinc n_{Zn}^{vac} vacancies in the (4×4) periodicity are shown. Previously stable oxygen vacancy structures are also shown.

formation of triangular reconstructions of length n involves the removal of $n \times (n+1)/2$ oxygen and $n \times (n-1)/2$ zinc atoms and corresponds to

$$n \times (n+1)/2 - n \times (n-1)/2 = n \qquad (13)$$

effective oxygen vacancies.

We see from Table V that the preferred vacancy concentration of a quarter of the oxygen surface atoms is only reached for triangular pits with a side length of three oxygen atoms, however, such structures are not favorable since the remaining islands are too small.

A way to increase the overall oxygen vacancy concentration for larger triangular pits is the removal of additional, smaller triangular-shaped reconstructions in the second double layer within the pit of the first double layer. We adopted the structures of the plain and nested triangles from Ref. 3 with oxygen and zinc atoms interchanged. The supercell size varied from

TABLE V. Smallest possible supercell $(m \times m)$ for triangular pits with side length n and the corresponding maximum oxygen vacancy concentration $c_{Ovac}^{triangle}$.

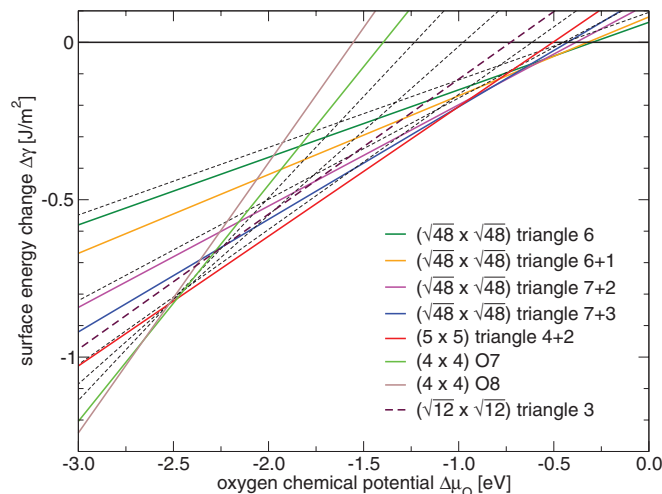| n	2	3	4	5	6	7
$(m \times m)$	$\sqrt{7}$	$\sqrt{12}$	$\sqrt{19}$	$\sqrt{27}$	$\sqrt{37}$	$\sqrt{48}$
$c_{Ovac}^{triangle}$	0.286	0.250	0.211	0.185	0.162	0.146

FIG. 9. (Color online) Surface energy as a function of the oxygen chemical potential for triangular reconstructions. The black dotted lines are the most stable phases found in Sec. III B. Triangular reconstructions are more stable than the previously found vacancy configurations for an oxygen chemical potential greater than -2.48 eV. For smaller chemical potentials, seven and eight oxygen vacancy structures remain the most stable structures.

(4×4) to $(\sqrt{48} \times \sqrt{48})$. As can be seen from Fig. 9, the triangular reconstructions are approximately 0.032 J/m^2 more stable than the simple vacancy configurations (black broken lines) at similar vacancy concentrations and at an oxygen chemical potential larger than -2.48 eV.

Although the triangular reconstruction with a side length of 3 and a supercell size of $(\sqrt{12} \times \sqrt{12})$ has the desired one quarter oxygen vacancy concentration, it is less stable than all other triangular reconstructions with approximately the same vacancy concentration. This indicates that larger triangles are generally preferred over small triangles, which is in agreement with the observations made for the Zn terminated (0001) surface side.[3] The (5×5) supercell with two nested 2 and 4 sized triangles in the surface layer has an oxygen vacancy concentration of 0.24 and comes closest to the desired 25%. It is by far the most stable triangular reconstruction $(-2.48$ eV $< \Delta\mu_O < -1.01$ eV).

At more oxygen-rich conditions, triangular reconstructions with a smaller oxygen vacancy concentration become more stable. In a $(\sqrt{48} \times \sqrt{48})$ supercell, two triangles with side lengths 7 and 3 $(c_{Ovac}^{triangle} = 0.208)$ and side lengths 7 and 2 $(c_{Ovac}^{triangle} = 0.1875)$ can be realized. Additionally, we also considered a simple triangle with side length 6 $(c_{Ovac}^{triangle} = 0.125)$, with and without an additional single oxygen vacancy in the triangular pit $(c_{Ovac}^{triangle} = 0.146)$ in the $(\sqrt{48} \times \sqrt{48})$ supercell. Under O poor conditions, on the other hand, the previously found surface reconstructions involving seven and eight vacancies remain the most stable structures since we were unable to determine triangular reconstructions with such a large vacancy concentration.

In Fig. 10, we added the triangular reconstructions to the phase diagram. As can be seen, all previously found reconstructions involving simple oxygen vacancies are higher in energy than the triangular reconstructions, except those with
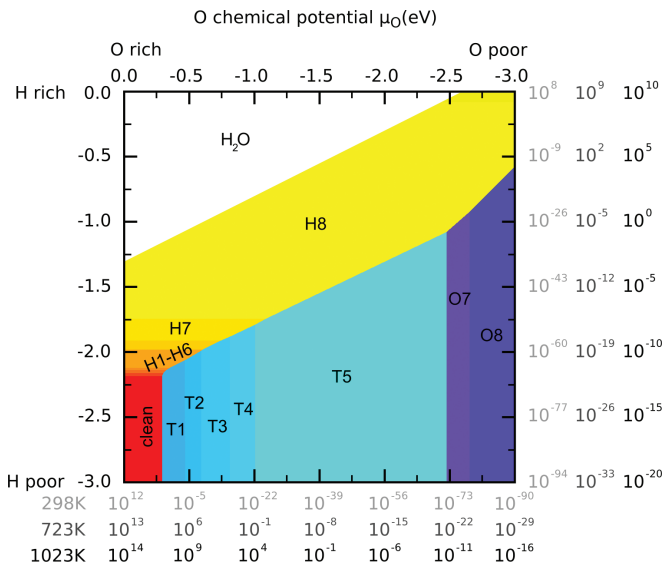
FIG. 10. (Color) Phase diagram including plain oxygen vacancies, hydrogen adatoms, oxygen and zinc vacancies, and triangular reconstructions. T1 = $(\sqrt{48} \times \sqrt{48})$ triangle $n = 6$, T2 = $(\sqrt{48} \times \sqrt{48})$ triangle $n = 6 + 1$, T3 = $(\sqrt{48} \times \sqrt{48})$ triangle $n = 7 + 2$, T4 = $(\sqrt{48} \times \sqrt{48})$ triangle $n = 7 + 3$, T5 = (5×5) triangle $n = 4 + 2$.

seven and eight oxygen vacancies. As a preliminary result, we can conclude that the triangular pits are more stable than oxygen vacancies. This is similar to the Zn terminated surface, where the triangular pits are the most stable reconstructions.[3]

F. Hexagonal holes

In the past, scanning tunneling microscopy (STM) was unable to reveal the atomic-scale structure of the O terminated $(000\bar{1})$ side of ZnO due to the weak conductivity of the surface at room temperature. Using integrated variable temperature STM, Lauritsen and co-workers[26] were able to investigate the surface reconstruction with atomic resolution at approximately 720 K (Fig. 11).
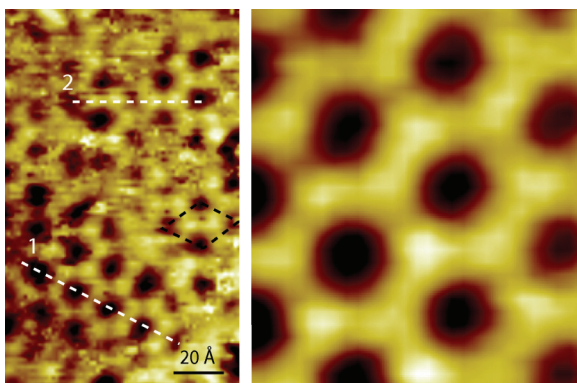

FIG. 11. (Color online) Left: High-resolution STM image (110 × 180 Å²) of the hexagonal (5×5) reconstruction structure present on the terrace planes recorded at ≈723 K. Right: Correlation averaged STM image (46 × 57 Å²) of the (5×5) reconstruction taken from Ref. 26.
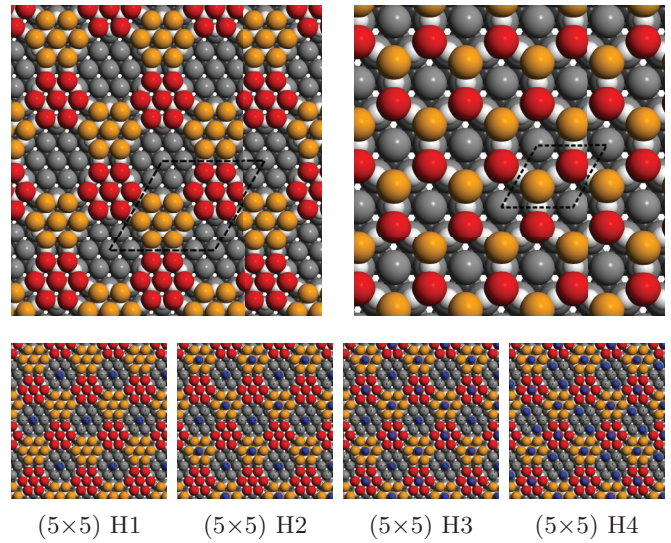

FIG. 12. (Color online) Schematic ball model of the most stable structure for the experimentally found hexagonal (5×5) supercell (left). Stoichiometric structure with a (2×2) periodicity (right), which is the most stable one at poor oxygen and hydrogen pressures. Oxygen atoms in the regular wurtzite stacking sequence are red color coded, whereas atoms at the atypical zinc-blende stacking sequence have orange color. Additionally, the supercells with different numbers of adsorbed hydrogen are presented for completeness.

The reconstruction is characterized by a sixfold symmetry with depressions (black color-coded areas) defining the center and the corners of the hexagon and six protrusions surrounding the center of the depression. The lattice parameter of the surface cell is measured to be 16.3 ± 0.02 Å, which is almost exactly five times the length of the in-plane unit cell of bulk ZnO ($a = 3.25$ Å). Therefore, the observed hexagonal honeycomblike structure can be recognized as a (5×5) reconstruction of the surface. Two characteristic properties for this particular termination of the $(000\bar{1})$ surface can be extracted from line scans indicated in Fig. 11 (see Ref. 26). The average depth of the depression relative to the bright regions is approximately 2.1 Å, which coincides well with the height of a single ZnO layer ($R_1 + R_2 = 2.6$ Å). The six protrusions exhibit an average height of 0.4 ± 0.1 Å relative to the region in-between them.

Taking into account the experimental findings, we performed extensive DFT calculations on the (5×5) supercell for a number of different surface models, which have to be compatible with the sixfold symmetry, a partial removal of the ZnO double layer, and the removal of approximately one quarter of the surface oxygen atoms for the electrostatic stabilization of the otherwise polar surface.

The most stable structure found is presented in Fig. 12. This surface reconstruction is modeled by removing 11 oxygen and 7 zinc atoms from the topmost layer of the $(000\bar{1})$ surface. With the remaining 14 oxygen atoms, 2 hexagons are formed, which are connected via fourfold-coordinated zinc ($4f$) atoms. One of these hexagons remains on the regular wurtzite ZnO stacking sequence (red atoms), whereas the other hexagon terminates the surface at the atypical zinc-blende stacking sequence (orange atoms). These two hexagon are interlinked by
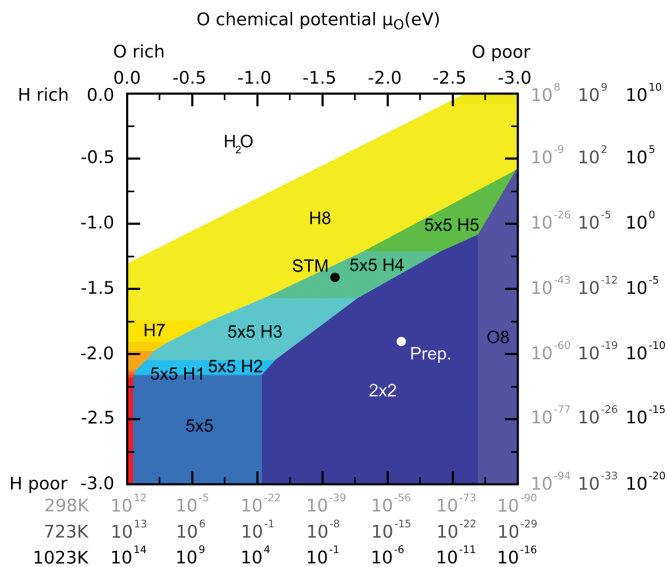
FIG. 13. (Color) Phase diagram of all considered reconstructions of the ZnO-(000$\bar{1}$) surface. Additionally, we indicate with filled circles the preparation conditions (1023 K) and the conditions where the STM image (Fig. 11) was recorded (723 K) with black dots.

threefold-coordinated zinc (3f) atoms to form a honeycomb-like structure with a one-layer hexagonal hole in the center.

As already mentioned before, it is necessary to remove one quarter of the oxygen surface atoms [in the case of a (5 × 5) supercell, this corresponds to $25/4 = 6.25 \approx 6$ atoms] to fully remove the polarity of O terminated ZnO surface. In this reconstruction model, only four more oxygen than zinc atoms are removed from the surface, and thus the surface polarity is not fully compensated. The remaining partial polarity of the (5 × 5) structure can be compensated by the formation of hydroxyl-groups (OH$^-$) on the surface. Up to five hydrogen atoms were adsorbed on the surface for compensation of the remaining 4.5 excess electrons.

Within our DFT calculations, we also identified a stoichiometric structure with a (2 × 2) periodicity to be more stable than previously discussed oxygen vacancies and triangular-shaped reconstructions at oxygen- and hydrogen-poor conditions. This structure is constructed along the same principles as the (5 × 5) structure. Two oxygen atoms and one zinc atom are removed from the surface layer and one of the remaining oxygen atoms is moved from the wurtzite to the zinc-blende stacking sequence. In contrast to the (5 × 5) structure, the (2 × 2) reconstruction fully compensates for the surface polarity without the need of additional hydrogen adsorbed at the surface. All oxygen atoms are interlinked by zinc atoms, which all possess an unusual threefold coordination to the oxygen atoms.

In Fig. 13, we finally present the phase diagram, which is based on all surface terminations taken under consideration so far. In comparison to the former phase diagram, we recognize the absence of the triangular-shaped vacancy structures, which are all higher in energy than the (2 × 2) (the large blue area) and (5 × 5) (light blue $c_H = 0$ to green $c_H = \frac{5}{25}$ areas) surface terminations.

As already mentioned in Ref. 26, inclusion of the two new reconstructions for the related polar (0001)-Zn surfaces

TABLE VI. Average heights of the terminating Zn and O surface atoms with respect to the neighboring O or Zn ions, respectively. All values are given in Å. "wurt." and "zinc" denote the stacking sequence of the first layer for the the (2 × 2) and (5 × 5) hexagonal hole reconstructions. Average heights from the first layer inside the hexagonal holes are denoted with "2nd layer." Also shown are the results for a single oxygen and zinc vacancy for a (2 × 2) surface cell.

	(0001) Zn terminated			(000$\bar{1}$) O terminated		
	wurt.	zinc	2nd layer	wurt.	zinc	2nd layer
(5 × 5) hex	0.33	0.35	0.28	0.53	0.56	0.48
(2 × 2) hex	0.33	0.34	0.34	0.54	0.57	0.67
(2 × 2) vac1	0.25			0.54		

did not modify the surface diagram for that surface, and the stability of the new hexagonal structures was already explained by the fact that the Zn atoms can be placed in a triangular environment, whereas O atoms prefer a tetrahedral coordination, in which all three O 2p orbitals can interact to form bonding and antibonding linear combinations. The more flexible Zn atom forms hybrid orbitals either using the d_{xz} and d_{yz} orbitals (tetrahedral) or the d_{xy} and d_{x2-y2} orbitals in the planar configuration. This is also confirmed by the height of the oxygen and zinc atoms in various reconstructions, which are summarized in Table VI.

Inspecting Table VI, we conclude that the O ions on the (000$\bar{1}$)-O surface clearly prefer a pyramidal coordination, protruding typically 0.5 Å above the three neighboring Zn ions, whereas the equivalent Zn ions on the (0001)-Zn surface can relax deeper into the surface and typically protrude only 0.3 Å. The flexibility of Zn coordination is essential for the observed stability of the (5 × 5) and (2 × 2) structures since $\frac{2}{3}$ or all of the surface Zn atoms, respectively, are placed in flat configurations with three neighboring O atoms being coplanar with the Zn atom. Hypothetical (5 × 5) and (2 × 2) structures on the Zn terminated surface would force O into a coplanar configuration with three neighboring Zn atoms, which is energetically very unfavorable.

IV. SUMMARY AND CONCLUSION

In this study, we have calculated the phase diagram of the (000$\bar{1}$)-O terminated surface of ZnO in dependence on the partial pressures of the two main constituents of the gaseous environment in the UHV chamber: oxygen and hydrogen. About 205 different surface terminations, including hydrogen adatoms as well as oxygen and zinc removal, have been considered. Honeycomblike surface terminations in (2 × 2) and (5 × 5) supercells were found to be energetically more favorable than triangular pits, which are the predominant surface terminations at the (0001)-Zn surface[3,4] at low temperatures.

In this work, we have reported many technical details, which were previously not discussed, as well as a detailed study of the different vacancy ordered structures and hydroxylated surfaces. Some intriguing observations were made for the oxygen vacancies on the (000$\bar{1}$)-O terminated surface of ZnO. As expected, a vacancy concentration of 25% is favorable over a wide range of oxygen chemical potentials. At this particular

vacancy concentration, the surface is essentially stoichiometric and all surface Zn and O atoms reach their full ionicity. We found that the remaining oxygen atoms prefer to arrange in such a manner that they are members of a honeycomb ring, but restriction to a 4×4 unit cell is somewhat limiting to make a final judgment on the precisely adopted patterns. One might argue that simple oxygen vacancy induced structures are merely an academic issue since the new (2×2) and (5×5) honeycomb structures are lower in energy. However, this work has entirely neglected vibrational as well as configurational entropy contributions, as well as kinetic limitations, which might stabilize the vacancy structure in practice in many experimental situations. Ideally, the present energetics should be combined with a careful cluster expansion and Monte Carlo simulations, as well as complemented by the inclusion of the vibrational entropy, to calculate a true finite-temperature phase diagram for ZnO surfaces. But, this is beyond the scope of the present density functional theory study.

Furthermore, we have investigated the formation of hydroxyl groups on the ZnO surface. As excepted, under hydrogen-rich conditions, hydroxylated surfaces are indeed stable (see large yellow area in Fig. 13). The interaction energy between OH groups is found to be very small compared to the interaction energy between oxygen vacancies. This suggests that configurational entropy might favor disorder even at relatively low temperatures. Again, a cluster expansion and treatment using MonteCarlo methods might yield interesting insight.

ACKNOWLEDGMENTS

[1] V. Srikant and D. R. Clarke, J. Appl. Phys. **83**, 5447 (1998).

[2] K. Ellmer, A. Klein, and B. Rech, *Transparent Conductive Zinc Oxide: Basics and Applications in Thin Film Solar Cells* (Springer, Berlin, 2008).

[3] G. Kresse, O. Dulub, and U. Diebold, Phys. Rev. B **68**, 245409 (2003).

[4] M. Valtiner, M. Todorova, G. Grundmeier, and J. Neugebauer, Phys. Rev. Lett. **103**, 065502 (2009).

[5] O. Dulub, U. Diebold, and G. Kresse, Phys. Rev. Lett. **90**, 016102 (2003).

[6] P. W. Tasker, J. Phys. C: Solid State Phys. **12**, 4977 (1979).

[7] C. Noguera, J. Phys.: Condens. Matter **12**, R367 (2000).

[8] O. Dulub, L. A. Boatner, and U. Diebold, Surf. Sci. **519**, 201 (2002).

[9] G. Kresse and J. Furthmüller, Comput. Mater. Sci. **6**, 15 (1996).

[10] G. Kresse and J. Furthmüller, Phys. Rev. B **54**, 11169 (1996).

[11] J. P. Perdew, J. A. Chevary, S. H. Vosko, K. A. Jackson, M. R. Pederson, D. J. Singh, and C. Fiolhais, Phys. Rev. B **46**, 6671 (1992).

[12] J. P. Perdew, J. A. Chevary, S. H. Vosko, K. A. Jackson, M. R. Pederson, D. J. Singh, and C. Fiolhais, Phys. Rev. B **48**, 4978(E) (1993).

[13] J. P. Perdew, K. Burke, and M. Ernzerhof, Phys. Rev. Lett. **77**, 3865 (1996).

[14] J. P. Perdew, A. Ruzsinszky, G. I. Csonka, O. A. Vydrov, G. E. Scuseria, L. A. Constantin, X. Zhou, and K. Burke, Phys. Rev. Lett. **100**, 136406 (2008).

[15] J. Heyd, G. E. Scuseria, and M. Ernzerhof, J. Chem. Phys. **118**, 8207 (2003).

[16] H. Sawada, R. Wang, and A. W. Sleight, J. Solid State Chem. **122**, 148 (1996).

[17] R. Wahl, D. Vogtenhuber, and G. Kresse, Phys. Rev. B **78**, 104116 (2008).

[18] J. Kiss, A. Witt, B. Meyer, and D. Marx, J. Chem. Phys. **130**, 184706 (2009).

[19] I. G. Batyrev, A. Alavi, and M. W. Finnis, Phys. Rev. B **62**, 4698 (2000).

[20] K. Reuter and M. Scheffler, Phys. Rev. B **65**, 035406 (2001).

[21] P. Raybaud, J. Hafner, G. Kresse, S. Kasztelan, and H. Toulhoat, J. Catal. **189**, 129 (2000).

[22] B. Meyer, Phys. Rev. B **69**, 045416 (2004).

[23] J. Paier, R. Hirschl, M. Marsman, and G. Kresse, J. Chem. Phys. **122**, 234102 (2005).

[24] M. Kunat, S. G. Girol, T. Becker, U. Burghaus, and C. Wöll, Phys. Rev. B **66**, 081402 (2002).

[25] C. Wöll, Prog. Surf. Sci. **82**, 55 (2007).

[26] J. V. Lauritsen *et al.*, ACS Nano **5**, 5987 (2011).

[27] M. van Hove and R. Leysen, Phys. Status Solidi A **9**, 361 (1972).